Journal of Geodesy (2021)95:66
https://doi.org/10.1007/s00190-021-01506-8

ORIGINAL ARTICLE

Comparison and evaluation of high-resolution marine gravity recovery via sea surface heights or sea surface slopes

Shengjun Zhang[1,2] · Adili Abulaitijiang[2] · Ole Baltazar Andersen[2] · David T. Sandwell[3] · James R. Beale[4]

Received: 19 September 2020 / Accepted: 26 March 2021

Abstract
There are two dominating approaches of modeling the marine gravity field based on satellite altimetry observations. In this study, the marine gravity field is determined in four selected areas (Northwestern Atlantic, Hawaii ocean area, Mariana Trench area, and Aegean Sea) by using exact same input datasets but different methods which are based on sea surface height (SSH) and sea surface slope (SSS), respectively. The impact of the methodology is evaluated by conducting validations with shipborne gravity observation. The CryoSat-2, Jason-1/2, and SARAL/Altika geodetic mission data (similarly 3-year-long time series) are firstly retracked by the two-pass retracker. After that, the obtained SSHs are used for the derivation of geoid undulations and vertical deflections, and then for the resulting marine gravity field separately. The validation results indicate that the SSH-based method has advantages in robustly estimating marine gravity anomalies near the coastal zone. The SSS-based method has advantages over regions with intermedium ocean depths (2000–4000 m) where seamounts and ridges are found, but obvious disadvantages when the ocean currents flow along the north–south direction (e.g., western boundary currents) or the topography features north–south directional trenches. In the deep ocean where the seafloor topography is plain and smooth, the two methods have similar accuracy.

Keywords Marine gravity anomaly · Geoid undulation · Vertical deflection · Satellite altimetry

1 Introduction

Over the past half-century, the technology of satellite earth observation has dramatically helped humans understand and model our planet better. Among them, satellite altimetry has proved to be an effective tool for observing surface heights with respect to a reference ellipsoid over oceans and land surfaces (Fu and Cazenave 2001; Stammer and Cazenave 2017). It is feasible to calculate marine gravity anomalies at global scale on the basis of altimeter measurements, e.g., sea surface height (SSH) (Andersen and Knudesen 1998; Andersen et al. 2010) or sea surface slope (SSS) (Sandwell and Smith 1997; Hwang et al. 2002).

The marine gravity field can be improved by incorporating more and more altimeter observations with enhanced range precision, complementary and denser spatial coverage, as well as diverse track orientations (Sandwell et al. 2013, 2014; Zhang et al. 2017, 2020; Zhu et al. 2020; Green et al. 2019). On top of that, these altimetry measurements from geodetic missions (GM) or long repeat orbit (LRO) missions (e.g., Geosat 1985–1986, ERS-1 1994–1995, Jason-1 2012–2013, CryoSat-2 2010–present, SARAL/AltiKa 2016–present, HY-2A 2016–present, Jason-2 2017–2019) provide the primary data source for mapping the marine gravity field (Sandwell et al. 2019; Zhu et al. 2019). Tailored waveform retracking is a mature and effective method to improve the range precision of existing altimeter observations, especially over marginal seas and sea-ice covered regions (McAdoo et al. 2013; Garcia et al. 2014; Khaki et al. 2015). In general, these marine gravity recovery studies are classified into two categories according to the calculation's dependence on

✉ Shengjun Zhang
zhangshengjun@whu.edu.cn

1 School of Resources and Civil Engineering, Northeastern University, Shenyang, China

2 DTU Space, Technical University of Denmark, Lyngby, Denmark

3 Institute of Geophysics and Planetary Physics, Scripps Institute of Oceanography, University of California San Diego, La Jolla, CA 92093, USA

4 National Geospatial-Intelligence Agency, 3838 Vogel Rd, Arnold, MO 63010, USA

Published online: 27 May 2021

either geoid undulations (SSH-based method) or vertical deflections (SSS-based method).

The geoid undulations are defined as the height of the geoid relative to a given reference ellipsoid. The SSHs are determined by using refinement of various corrections due to path delay of signal or geographic environment of ocean surface, as well as crossover adjustment in order to suppress the effect of radial orbit error. The SSH-based method enables a determination of the mean sea surface (MSS) model along with the marine gravity model. In this method, the relationship between marine gravity anomaly and geoid undulation is established by the inverse Stokes equation (Hofmann-Wellenhof and Moritz 2005).

Vertical deflection, the angle between the plumb line of geoid and the normal line of the reference ellipsoid, is another intermediate and critical variable for marine gravity recovery. It is usually decomposed into two mutually perpendicular components: the north–south (ξ), positive toward the north, and the east–west (η), positive in the east direction (Barzaghi et al. 2016). The vertical deflection is calculated from the SSS. The SSS is calculated from the along-track difference procedure, which has advantages such as crossover adjustment not being necessary for the SSS-based method (Olgiati et al. 1995). Several corrections have a negligible level of effect on calculating SSS, e.g., radial orbital error, dry tropospheric path delay, solid earth tide correction, and geocentric polar tide effect (Zhang et al. 2018). An issue with the SSS-based method is that the two directional components have different accuracy over different latitudinal zones. For instance, the estimated east–west component η has almost 3 times larger uncertainties than ξ at low-latitude zones as an altimeter generally flies north–south (close to 90° inclinations) (Sandwell and Smith 1997). The relationship between marine gravity anomaly and vertical deflection is established by the inverse Vening–Meinesz formula (Hwang 1998) and the Laplace equation (Sandwell and Smith 1997).

Both methods have advantages and disadvantages, and this paper aims to evaluate the performance of the SSH-based method and the SSS-based method over typical ocean areas. It is well known that such analysis cannot cover all possible conditions, but we aim to discuss this for a number of study areas. The Northwestern Atlantic (20°–90°W, 20°–55°N) is selected as a major study region with obvious influence of the Gulf Stream and typical features of seafloor topography including ridges and fracture zones. The Aegean Sea (22°–28°E, 35°–41°N), the Hawaii area (152°–172°W, 15°–30°N), and the Mariana area (138°–145°E, 30°–43°N) are chosen to further distinguish method-derived differences over regions with a complex coastline and shallow water, steep seamounts, and deep water, and an extremely deep ocean trench, respectively.

For the altimetry, we process the GM/LRO data from CryoSat-2, Jason-1/2, and SARAL/Altika. The two-pass waveform retracker has been proved to be an effective strategy for improving the range precision of traditional low-resolution-mode measurements by a factor of 1.5–1.7 (Sandwell et al. 2005,2019; Garcia et al. 2014; Zhang and Sandwell 2017). We uniformly adopt the two-pass retracker in this study. Based on the same multi-satellite altimetry dataset, the grids of marine gravity anomalies will be predicted, evaluated, and compared for both high-resolution gravity recovery methods. There are only a few papers comparing and evaluating the pros and cons of different methods for marine gravity field retrieval. Olgiati et al (1995) used data from Geosat, ERS-1, Topex-Poseidon exact repeat mission (ERM), and Geosat GM (south of 30°S) and came to a conclusion which is likely outdated. Today, there are more than 10 years of geodetic missions, and the accuracy levels of SSHs are significantly improved in the past 25 years. Therefore, a more comprehensive conclusion is sought here. This paper follows in the footprints of Olgiati et al (1995). We focus on a much more detailed evaluation of the methods for marine gravity recovery. The analysis is valuable for the derivation of earth gravity models (EGMs) (Pavlis et al. 2012) together with satellite altimetric gravity anomalies, which aims to perform the optimal integration of regional datasets in preparation for next–generation EGMs.

The remainder of this paper is organized as follows. Section 2 provides general description of the datasets, e.g., study areas and shipborne marine data, altimeter data and retracking, as well as other altimetric models for the purpose of comparison. The theoretical background of the gravity recovery methods is presented in Sect. 3. Section 4 presents the comparative performance evaluation of two high-resolution gravity recovery methods over study areas. We will also perform analysis over a number of subregions with specific geological/oceanographic features to support conclusions in Sect. 5.

2 Data description

2.1 Study areas and marine data

A high-quality shipborne dataset is essential to provide objective evaluation for marine gravity recovery studies. Shipborne gravimetry is a conventional method to measure the marine gravity field, and its measurements have special advantages including high-accuracy and high-resolution compared to observations from satellite altimetry (Lu et al. 2019). Marine data are widely used as input data for constraining gross errors or verification data in marine gravity recovery studies (Li et al. 1997; Catalao 2006; Stenseng and Andersen 2012; Zaki et al. 2018). In general, shipborne

marine data provide independent assessment of altimetry-derived marine gravity anomalies but is limited to areas where data are available and accessible. The four study areas, marked within black rectangular boxes in Fig. 1a, are selected based on the availability of high-quality shipborne gravity measurements and typical characteristics for marine gravity anomaly distributions.

Over the Northwestern Atlantic area, a high-precision dataset, with assessed accuracy superior better than ~ 2 mGal, is collected and archived from the cooperation with the National Geospatial-Intelligence Agency (NGA). This high-accuracy level leads to a more reasonable verification to evaluate the performance of marine gravity recovery methods. On top of that, the NGA's dataset is already used while constructing the EGM2008 model. Over 1.4 million measurements are distributed densely along the coast, and their trajectories are shown in Fig. 1b. The standard deviation (STD) of marine gravity anomalies is ~ 28.6 mGal. In this region, the Gulf Stream flows along the Northwestern Atlantic shelf, and the sea shelf increases the sea level variability in large parts of the region.

Over the Hawaii ocean area, 153,578 measurements are collected through NGA. Hundreds of seamounts are distributed in this region, and the STD of marine gravity anomalies is ~ 45.4 mGal. Over the Aegean Sea with its complicated coastal environment, only 19,645 observations are available from the GEOMED2 project (Barzaghi et al. 2019), where the marine gravity observations were used to determine the geoid for the Mediterranean Sea. The southern Aegean Sea shows very uniform, high gravity anomalies of about 100 mGal, which appear to decrease gradually to the north, northeast, and northwest (Harrison 1955). Besides, the southwest corner of this study area is characterized by very large negative anomalies. Therefore, the STD of marine gravity anomalies is ~ 60 mGal. The Mariana area features a very deep trench, and altimetry measurement precisions are often influenced by the strong Kuroshio current crossing the region. The STD of marine gravity anomalies is around 90 mGal, and 190,825 shipborne measurements are accumulated by NGA. The geographic distribution and the numerical values of shipborne measurements are shown in Fig. 1c–e. We did no additional editing for these shipboard data in this study.

2.2 Altimeter data

Both Jason-1 (2001–2013) and Jason-2 (2008–2019) operated in a geodetic mission during their end-of-life phase. Jason-1 provided a 410-day-long time series of observations, including one complete GM cycle of ~ 406 days,

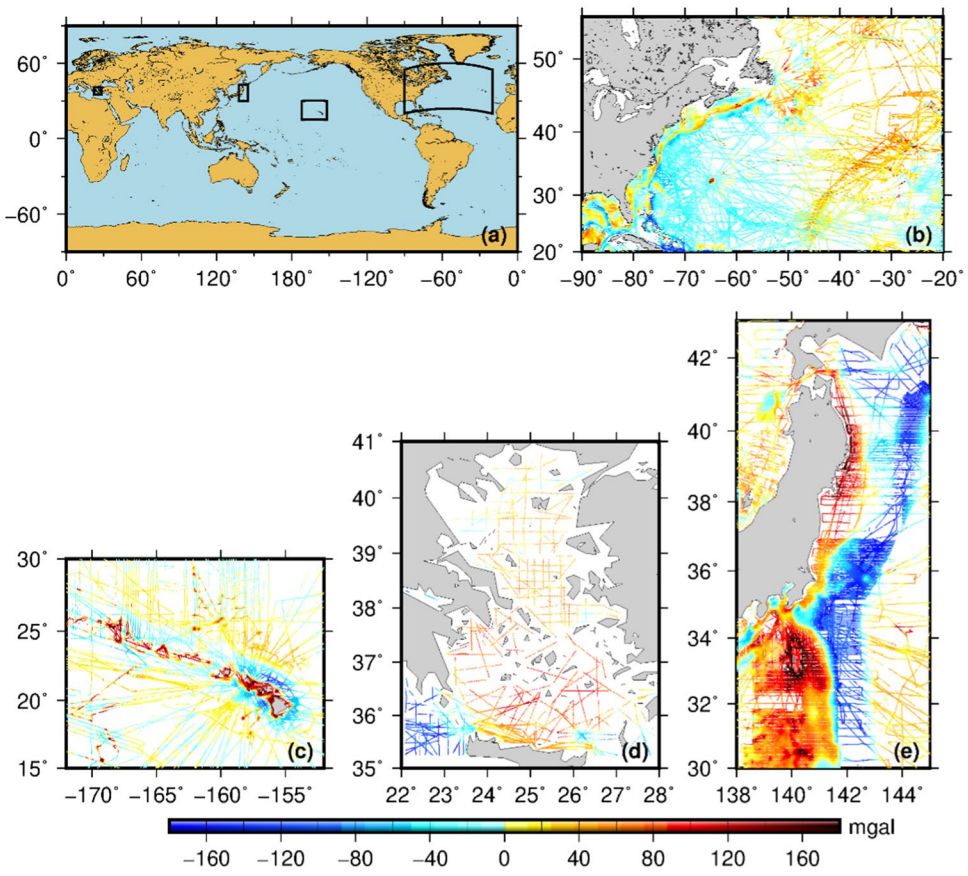

Fig. 1 Geographic distribution and marine gravity anomaly values of shipboard measurements within selected study areas: **a** study areas are marked within rectangles; **b** marine data over the Northwestern Atlantic; **c** marine data over the Hawaii area; **d** marine data over the Aegean Sea; **e** marine data over the Mariana area

and the cross-track spatial distances reach ~ 8 km at the equator. Jason-2 conducted two complete LRO cycles of ~ 371 days, and accumulated measurements with cross-track spatial distance at around 4–5 km.

The SARAL/AltiKa (2013–) is operating in a GM mode since July 2016 and is accumulating a more than 3-year-long time series of observations. The orbit of SARAL/AltiKa drifts, and the data distribution is not as even as Jason-1 or Jason-2.

CryoSat-2 also provides high-quality SSH measurements with a long repeating period of ~ 369 days and thus dense data distribution. More than 9 years of CryoSat-2 (2010–) data are collected with cross-track sampling of ~ 8 km. While CryoSat-2 operates in three modes over different earth surfaces, the traditional low-resolution mode (LRM) is adopted over most open ocean areas. Hence, we adopt 3.5-year-long time series of LRM observations as the sample dataset in our study by considering the similar time series lengths with those of Jason-1/2 and SARAL/AltiKa.

The Sensor Geophysical Data Record (SGDR) products for Jason-1 GM, Jason-2 GM, and SARAL/AltiKa GM are obtained from the Archiving, Validation, and Interpretation of Satellite Oceanographic (AVISO) data service. The L1b-level products for CryoSat-2 LRM are acquired through the data distribution service of the European Space Agency (ESA). All these products include along-track high-sampling-rate waveforms (e.g., 20 Hz for Jason-1, 40 Hz for SARAL/AltiKa).

The dense along-track sampling (~ 0.35 km and ~ 0.18 km for 20 Hz and 40 Hz data, respectively) and cross-track sampling (~ 4 km at best) enable construction of the high-resolution gravity field model. We design our experiments on the basis of measurements from these four missions to evaluate two different gravity recovery methods.

The specific information for the acquired altimetric dataset is listed in Table 1.

The geographical distributions of altimetric observations for Jason-1, Jason-2, SARAL/AltiKa, and CryoSat-2 LRM are shown over the Bermuda region (60°–66°W, 31°–34°N) in the Northwestern Atlantic in Fig. 2. All these altimeter missions provide a dense spatial distribution. Among them, the ground tracks for Jason series have the most even distribution and smallest cross-track sampling, although a small proportion of data is unavailable due to safe-holds.

Here, we use the standard L1B products from Jason-1 GM, Jason-2 GM, SARAL/AltiKa GM, and CryoSat-2 LRM including waveforms. The along-track rough SSHs are obtained by subtracting 20 Hz on-board tracked range measurements from 20 Hz altitude (40 Hz for SARAL/AltiKa). Then, range corrections are added based on waveform retracking strategies which are described in Sect. 2.3. The relevant environmental and geophysical corrections of the altimeter range measurements have been applied to calculating SSHs. These corrections include dry and wet tropospheric path delay, ionospheric correction, sea state bias, ocean tide, solid earth tide, pole tide, high-frequency wind effect, and inverted barometer correction. All these corrections are provided in the standard products for the four altimeter missions, and no extra updating procedure is applied. Only 1 Hz correction items are provided in the original products. Hence, we interpolate all these 1 Hz items into 20 Hz or 40 Hz by using piecewise cubic spline interpolation in order to match the high-sampling-rate measurements.

2.3 Retracking

Waveform retracking is an effective strategy to improve the range precision of altimeter echoes. A variety of waveform retracking algorithms have been proposed on the basis of empirical or physical models. An empirical retracker has advantages in providing valid and robust estimation for almost all types of waveforms, even for those collected from complicated reflecting surfaces. Physical retrackers usually calculate objective parameters by fitting echoes to a certain waveform model, e.g., Brown model (Brown 1977). These physical methods have advantages in estimating parameters for both range corrections and sea state conditions, e.g., significant wave height and wind speed.

Over the ocean, the typical shapes of raw waveforms from all four satellite missions are well-modeled using the Brown-type model with five parameters: arrival time, rise time, amplitude, square of the antenna mispointing angle, and thermal noise. Considering the inherent relationship between the errors in retracked estimates of arrival time and rise time, the two-pass waveform retracker estimates arrival

Table 1 The general information for acquired altimeter data sets

Mission	Time scope	Cycle range	Orbital inclination	Cross-track distance
Jason-1 GM	20120507–20130621	C500–C537	66°	~ 8 km
Jason-2 GM	20170711–20191001	C500–C537 C600–C644	66°	4–5 km
SARAL/AltiKa GM	20160704–20191111	C100-C134	98.5°	N/A
CryoSat-2 LRM	20100716–20131228	C004–C048	92°	~ 8 km

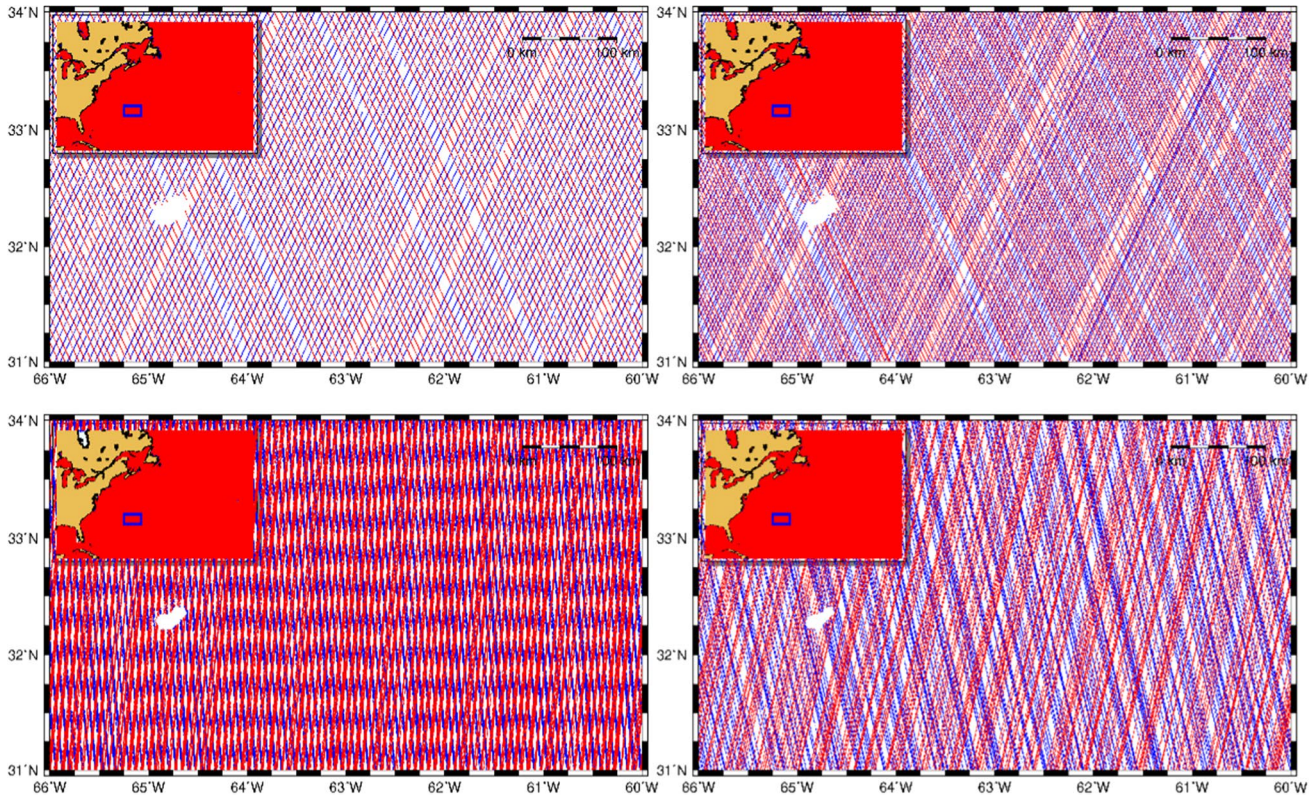

Fig. 2 Geographic distribution of multi-satellite altimeter measurements during geodetic missions with dense ground tracks. Upper left: Jason-1; upper right: Jason-2; bottom left: CryoSat-2 LRM; bottom right: SARAL/AltiKa

time with higher precision by fixing the rise time parameter in one more model-fitting procedure (Sandwell et al. 2005; Sandwell and Smith 2009; Zhang et al. 2017, 2020). In the first step, the waveforms are fitted by the three-parameter Brown model (arrival time, rise time, and amplitude). The thermal noise and square of the antenna mispointing angle are treated as constant parameters but need suitable predetermination. In the second step, the rise time parameter is smoothed along-track and fixed, before retracking the waveforms again using a two-parameter Brown model (arrival time and amplitude). Either the former three parameters or the latter two parameters will be solved during a weighted least squares procedure. This approach has been proved effective for these four missions in our study: Jason-1, Jason-2, SARAL/AltiKa, and CryoSat-2/LRM (Garcia et al. 2014; Zhang and Sandwell 2017).

To evaluate the performance of waveform retrackers, we investigated 20 Hz or 40 Hz SSH for the four missions by removing the Dynamic Ocean Topography (DOT) effect. The STD of all SSH observations within a one-second interval is a measure of the measurement noise or the range precision. The red histograms of the noise level after the two-pass retracking procedure for diverse missions are shown in Fig. 3. The noise distribution of RADS (Radar Altimeter Database System) altimetry data is also outlined by the blue histograms for comparison.

As shown in Fig. 3, the two-pass retracker gives less (along-track) altimetry measurement noise compared to the modified Brown retracker implemented in RADS. SARAL/Altika is proved to be very important for gravity field recovery (Sandwell et al. 2019). Among the four satellites, SARAL/Altika measurements have the best range precision (average ~ 0.025 m), and an improvement of nearly a factor compared to, e.g., the Jason series (average ~ 0.04 m).

2.4 Altimetry derived marine gravity models

We introduce the latest published altimetry derived marine gravity models for comparison and verification. The most well-known and widely accepted global marine gravity models can be classified into two groups. The DTU17 (Andersen and Knudsen 2019) global gravity field model, as well as its predecessors (Andersen et al. 2014), are released by the Technical University of Denmark (DTU). Meanwhile, the Sandwell and Smith (SS) series of global marine gravity models (e.g., V27.1), including its predecessors, are released by the Scripps Institution of Oceanography (SIO). The DTU marine gravity modeling applies the inverse Stokes method

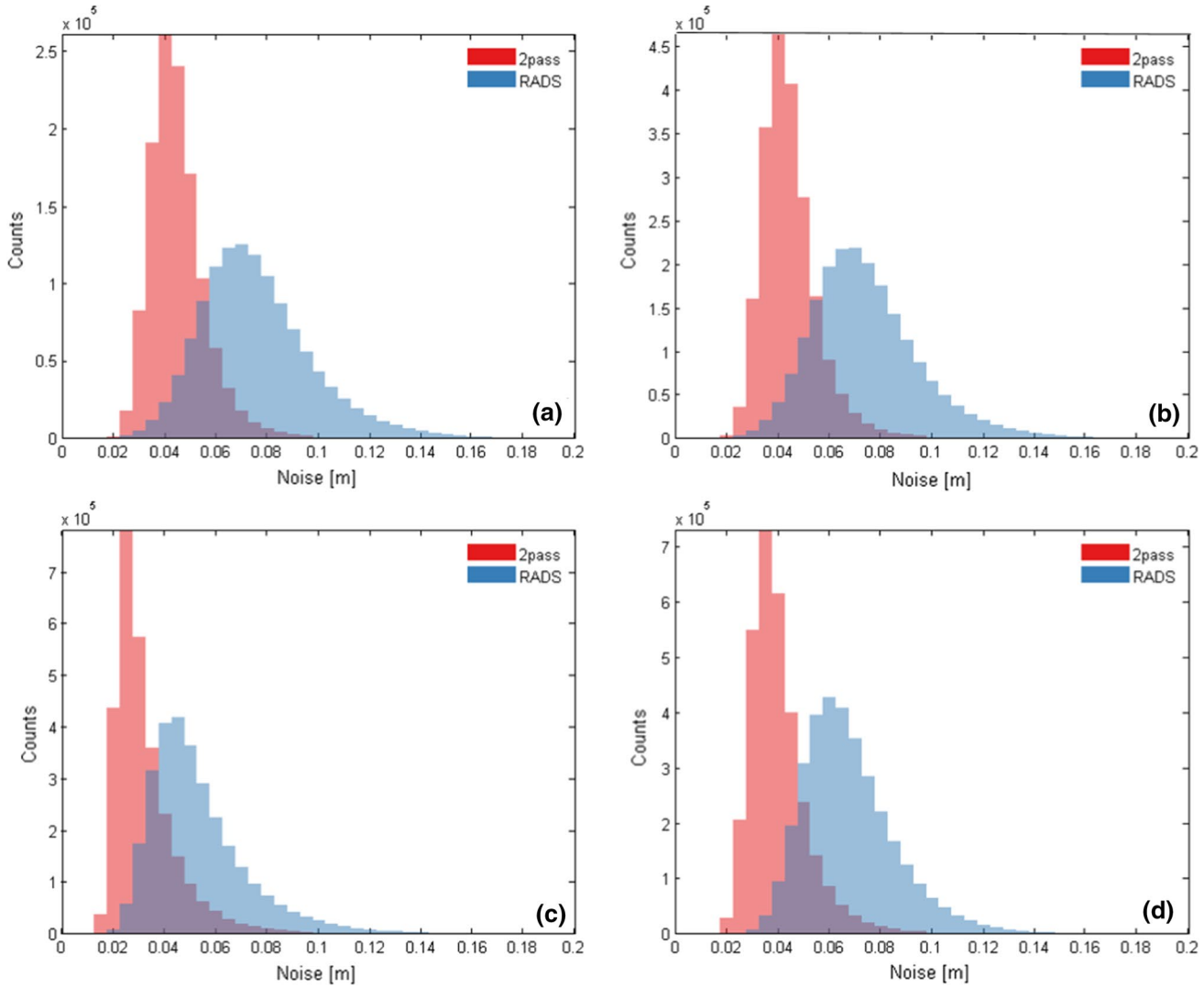

Fig. 3 Sea surface height (anomaly) noise for 1 Hz observations for different satellites: **a** Jason-1, **b** Jason-2, **c** SARAL/Altika, **d** CryoSat-2 in the study area Northwestern Atlantic. Red indicates two-pass retracked data. The noise characteristics of RADS altimetry data are also outlined by the blue histograms

directly to altimetry determined geoid undulation (derived from SSH), see Sect. 3.1, while the SIO marine gravity modeling applies the Laplace equation to deflection of verticals (derived from SSS), see Sect. 3.2. Both methods apply Fast Fourier Transform (FFT) algorithms in calculation under the flat earth approximation. These models incorporated as many altimetric measurements as possible by the year of their release.

For these involved global models, the duration of observations for the four altimetric missions is listed in Table 2. Besides these four missions, the global grids also adopted different amounts of multi-satellite altimetric datasets, e.g., Geosat GM/ERM, ERS GM/ERM, Envisat, T/P, T/P tandem, Jason-1/2 ERM, SARAL/AltiKa ERM, and CryoSat-2 SAR/SIN.

Table 2 Amount (approximately in months) of data for the altimetric missions

Mission	DTU17	V27.1	This study
Jason-1 GM	~14	~14	~14
Jason-2 GM	0	~12	~26
SARAL/AltiKa GM	~12	~25	~40
CryoSat-2 LRM	~84	~96	~40

3 Methods for gravity anomaly computation

3.1 Gravity anomalies from geoid undulations

The gravity prediction is conducted by the remove-restore method which is commonly used in the field of geoid determination (Featherstone et al. 2004; Yildiz et al. 2012). Initially, predicting gravity anomalies from SSHs is an inverse process of geoid determination. The anomalous potential T, geoid N, and gravity anomaly are related by the fundamental equation of geodesy and Brun's formula,

$$\Delta g = -\frac{\partial T}{\partial r} - \frac{2T}{r}, \quad \text{with} \quad T = \gamma_0 * N \tag{1}$$

where γ_0 is the normal gravity.

The satellites measure the sea surface heights. The SSH can be described by the sum of geoid height N, dynamic ocean topography (DOT) $\varepsilon_{\mathrm{DOT}}$, and other time-varying components $\varepsilon(t)$ and error e.

$$\mathrm{SSH} = N + \varepsilon_{\mathrm{DOT}} + \varepsilon(t) + e \tag{2}$$

The geoid N can be further represented by the known geoid heights from a reference model and a residual geoid signal ΔN. In this study, the geoid from EGM2008 (Pavlis et al. 2012) is used as a reference model, which is also used in the development of the global grids (e.g., DTU17 and V27.1). The DOT2008A_n180 model, which is complete to degree and order (d/o) 180 and associated with EGM2008, is adopted to calculate ε_{DOT}. The residual gravity field is determined from the residual geoid signal, and the full wavelength gravity is recovered by adding back the gravity field provided by the same reference model. For the detailed computation procedure, refer to Andersen and Scharroo (2011).

3.2 Gravity anomalies from vertical deflections

The relationship between vertical deflections and gravity anomalies can be deduced by the Laplace equation (Sandwell and Smith 1997). The details of the relationships are established according to the internal connections among the disturbing potential T, gravity disturbances δg, gravity anomaly Δg, and two directional components of vertical deflections (ξ and η). Assuming a flat earth approximation, the disturbing potential T satisfies the Laplace equation in the given local planar coordinate system (x, y, z). Then, the relationship between gravity and vertical deflection can be established as the following equation.

$$\frac{\partial \delta g}{\partial z} = -\gamma_0 \left(\frac{\partial \xi}{\partial x} + \frac{\partial \eta}{\partial y} \right) \tag{3}$$

Taking the difference between gravity disturbance and gravity anomaly into account, the gravity anomaly is further calculated according to,

$$\Delta g(x, y) = \delta g(x, y) - 2\frac{\gamma_0}{R} N(x, y) \tag{4}$$

where R is the average radius of Earth, and N is the geoid height, which can be provided by geo-potential models. For the detailed computation procedure, refer to Zhang et al. (2020).

4 Results and discussions

4.1 Gravity anomaly computation

On the basis of along-track obtained SSHs from four missions at high sampling rate (20 Hz or 40 Hz), we, respectively, calculate marine gravity anomalies relying on two different methods. We try to keep the methods as close as possible and resembling to the methods used for deriving the DTU and SIO models.

For the SSH-based method, the EGM2008 geoid is removed from the high-rate along-track SSHs, and absolute height anomalies over 2 m are flagged as outliers. A 21-point (41 for SARAL/Altika) moving average window is applied to the height anomalies. The STD of the points used for averaging is saved as the "noise" for a specific location. Besides the noise, the valid number of points used for averaging is also saved and later used for filtering height anomalies. In this study, the high-rate altimetry data are down-sampled to 1 Hz after along-track filtering. We only use height anomalies obtained by averaging at least 15 valid observations and with STD lower than 10 cm for the data retracked by the two-pass retracker. The DOT2008A is further subtracted to remove the medium to long wavelength signal from the height anomalies. For each individual track, bias and tilt terms are estimated from the residual height anomalies to reduce the effects of residual orbit errors and dynamic sea state variability. Then, all tracks are crossover adjusted (Knudsen and Brovelli 1993) using bias and tilt terms. Residual gravity anomalies are computed from gridded residual height anomalies using the FFT method (Forsberg and Sideris 1983; Schwarz et al. 1990) and a filter radius of 8 km. In the final step, EGM2008 gravity anomalies are added to restore the full gravity field.

For the SSS-based method, we uniformly resampled 20 Hz or 40 Hz data along profiles into ~ 5 Hz rate. After that, the along-track sea surface height gradients are calculated, while the along-track gradients of the EGM2008 model are also interpolated for a preliminary verification to detect outliers. Considering that the high-frequency noise was amplified during the difference procedure, we used

Parks–McClellan low-pass filters in order to obtain along-track filtered sea surface height gradient data (Zhang et al. 2017). The filter has a 0.5 gain at ~ 6.7 km, which is approximately consistent with the spatial interval of down-sampled 1 Hz data in SSH-based method. Then, the DOT2008A_n180 and EGM2008 model are, respectively, subtracted from along-track sea surface height gradients. The along-track residual vertical deflections were computed through dividing by estimated on-orbit velocity for different satellites. After that, the directional components of residual vertical deflection at grid points were calculated. Then, the residual gravity anomalies were calculated using the FFT method according to the relationship formula between gravity anomaly and vertical deflection. Different from V27.1 model which adopted depth-dependent filters (0.5 gain wavelength ranges from 13 to 20 km), a 2-D low-pass filter with a fixed 0.5 gain wavelength radius at 8 km is applied here. The fixed value is chosen to be consistent with filter radius (8 km) used in the SSH-based method. At last, marine gravity anomalies are inversed after restoring the reference EGM2008 model which was removed before.

4.2 Evaluation

We quantitatively evaluated the calculated marine gravity anomalies derived from the two methods by investigating statistics of misfit between altimetry-derived results and shipborne gravity measurements in Table 3. These in situ observations were further divided into three groups with different ranges of distances to the coast, and the separate statistics are listed as well. In this study, the coastal zone is roughly selected within 15–50 km to the nearest coastline, while the nearshore is selected where the distance to the coast is less than 15 km. Distance to coast larger than 50 km is regarded as open ocean.

The overall conclusions are that the SSH-based method outperforms over coastal areas, while the SSS-based method has advantages over open ocean areas. The SSH-based method has advantages in the nearshore regions, showing improvements by ~ 2 mGal in Northwestern Atlantic and Hawaii region. The enhanced rate of data loss and uneven distribution of available measurements have larger influence on the SSS-based method than on the SSH-based method. Besides, the improvement is obvious and significant as the offshore distance increases for both methods. This regularity is consistent with the statistics from the DTU17 and V27.1 models, respectively.

The ratio of in situ data over open ocean is too high and requires further division in order to consider more specific cases, e.g., trench with different directions, seamounts, complex or plain seafloor topography, high or low ocean variability, and so on. Hence, the comparison and statistics with shipborne gravity data in Table 3 provide an overall assessment between the two methods and further discussion will follow up in Sect. 4.3.

Table 3 Validation information of shipboard data with respect to results derived from two methods

Ocean area	Description	STD of height anomaly/m	Count of altimeter data	Count of marine data	SSS-based method	SSH-based method	EGM08	DTU17	V27.1
Northwestern Atlantic	Entire	–	–	1,409,700	3.113	2.787	2.883	2.642	3.005
	0–15 km	0.419	122,990	59,946	4.679	3.031	2.667	2.632	5.022
	15–50 km	0.412	347,936	170,768	3.623	2.919	2.779	2.640	3.531
	50 + km	0.431	8,837,064	1,177,745 (83.5%)	2.877	2.733	2.899	2.632	2.736
Hawaii	Entire	–	–	153,578	5.507	5.214	5.520	5.175	5.445
	0–15 km	0.123	8314	7953	12.892	10.468	10.562	10.264	13.121
	15–50 km	0.121	37,936	15,915	6.934	6.862	7.056	6.583	6.863
	50 + km	0.141	1,874,265	129,489 (84.3%)	4.337	4.384	4.779	4.423	4.234
Mariana	Entire	–	–	190,825	5.923	5.876	6.203	5.817	5.697
	0–15 km	0.263	23,484	11,409	9.201	8.608	9.106	8.765	9.145
	15–50 km	0.327	62,255	39,936	6.239	6.175	6.452	6.157	6.020
	50 + km	0.524	378,578	139,318 (73.0%)	5.443	5.494	5.808	5.386	5.190
Aegean	Entire	–	–	19,645	5.673	5.623	7.052	6.261	6.031
	0–15 km	0.137	27,951	7375	7.005	6.241	8.186	7.324	7.680
	15–50 km	0.103	27,846	9418	4.947	5.469	6.408	5.725	5.040
	50 + km	0.095	6685	2852 (14.5%)	3.748	4.257	4.997	4.449	3.682

The first and second columns show different study areas and further division by the distance to coast. The third, fourth, and fifth columns, respectively, indicate STD of height anomalies, count of altimeter observations, and count of shipboard measurements. The last five columns show validation results of shipboard with different grids of gravity anomalies, and the unit is mGal

Table 4 Validation information of shipboard data with respect to results within different ranges of ocean depths

Ocean area	Ocean depth	STD of Height anomaly/m	Count of altimeter data	Count of marine data	SSS-based method	SSH-based method	EGM08	DTU17	V27.1
Northwestern Atlantic	0–50 m	0.350	204,135	190,158	3.491	2.489	2.121	2.157	3.564
	50–200 m	0.214	403,367	114,222	3.037	2.586	2.608	2.438	2.977
	200–2000 m	0.461	693,671	201,605	3.592	3.112	3.146	2.906	3.475
	2000–4000 m	0.450	2,841,956	491,959	2.857	2.798	3.076	2.692	2.721
	4000 + m	0.331	5,164,968	410,965	2.859	2.731	2.862	2.674	2.694
Hawaii	0–50 m	0.117	3001	754	9.179	8.335	8.306	8.003	9.101
	50–200 m	0.124	2100	1380	14.759	10.850	11.665	11.296	14.903
	200–2000 m	0.127	31,380	16,464	9.870	9.207	9.635	8.984	9.851
	2000–4000 m	0.129	123,356	22,882	5.676	5.786	6.227	5.573	5.537
	4000 + m	0.140	1,760,657	111,905	4.056	3.980	4.223	4.035	3.987
Mariana	0–50 m	0.193	5328	1270	9.999	8.978	9.312	9.126	10.823
	50–200 m	0.204	21,482	5583	9.535	9.088	9.038	9.030	9.472
	200–2000 m	0.398	104,099	78,178	6.188	6.351	7.012	6.400	5.926
	2000–4000 m	0.480	124,772	66,913	4.828	4.829	5.046	4.694	4.586
	4000 + m	0.512	208,664	38,726	6.089	5.764	5.564	5.540	5.827
Aegean	0–50 m	0.155	1308	16	3.948	3.540	6.425	6.273	5.072
	50–200 m	0.146	10,777	895	7.881	6.573	9.352	9.052	7.367
	200–2000 m	0.115	41,545	15,077	5.894	5.766	7.290	6.403	6.386
	2000–4000 m	0.099	8374	2626	3.884	4.569	5.217	4.648	3.685
	4000 + m	0.099	692	1031	3.461	3.873	4.452	3.968	3.458

The first and second columns show different study areas and further division by the ocean depth. The third, fourth, and fifth columns, respectively, indicate STD of height anomalies, count of altimeter observations, and count of shipboard measurements. The last five columns show validation results of shipboard with different grids of gravity anomalies, and the unit is mGal

Similar statistics were performed by considering five groups of ocean depths. STDs of height anomalies and difference with respect to marine data are listed in Table 4. In general, the SSH-based method gets smaller STDs than the SSS-based method over shallow water areas (0–50 m) and shelf areas (50–200 m), while both methods have similar and comparable performance over the shelf break (200–2000 m) and deep ocean (4000 + m). Besides, the SSS-based method has advantages over zones with intermedium ocean depths (2000–4000 m) where seamounts and typical seafloor structures are found. However, the uniform division of ocean depth range is not always reasonable for the four study regions. For example, over 90% of altimeter observations are distributed at deep ocean areas (4000 + m) in Hawaii. Hence, further discussion in Sect. 4.3 is also necessary based on small characteristic subregions.

4.3 Characteristic subregions

The geographical distribution maps of final marine gravity anomalies after the remove-restore procedure are hard to distinguish between two methods. Hence, we plot the distribution of residual gravity anomalies with respect to EGM2008 to distinguish the two methods. Besides, the marine gravity anomalies and ocean depths are, respectively, plotted on the basis of the EGM2008 and GEBCO_2020 (GEBCO Bathymetric Compilation Group 2020) models. The detailed results within the four study areas are separately shown in Figs. 4, 5, 6, and 7.

The residual signals are generally consistent with slightly different features for the two methods. For the Northwestern Atlantic (Fig. 4), both the western boundary current and the Mid-Atlantic Ridge are apparently detected in the residual signals. The SSS-based method has strong signals over the drainage area of the western boundary current and is more easily influenced by high ocean variabilities. For the Hawaii region (Fig. 5), the signals around seamounts and islands are strong for both methods, whereas the SSS-based method has ground track patterns of altimeter observations. For the Mariana Trench area (Fig. 6), the central part of study region has obviously different residual signals for the two methods. The major differences can be attributed to residual long-wavelength oceanographic signals residing in slope gradients and high ocean variability due to the Kuroshio. For the Aegean Sea (Fig. 7), the residual signals of the SSS-based method are larger over the northern Aegean Sea and the southwest corner of the study region. The signals of the SSH-based

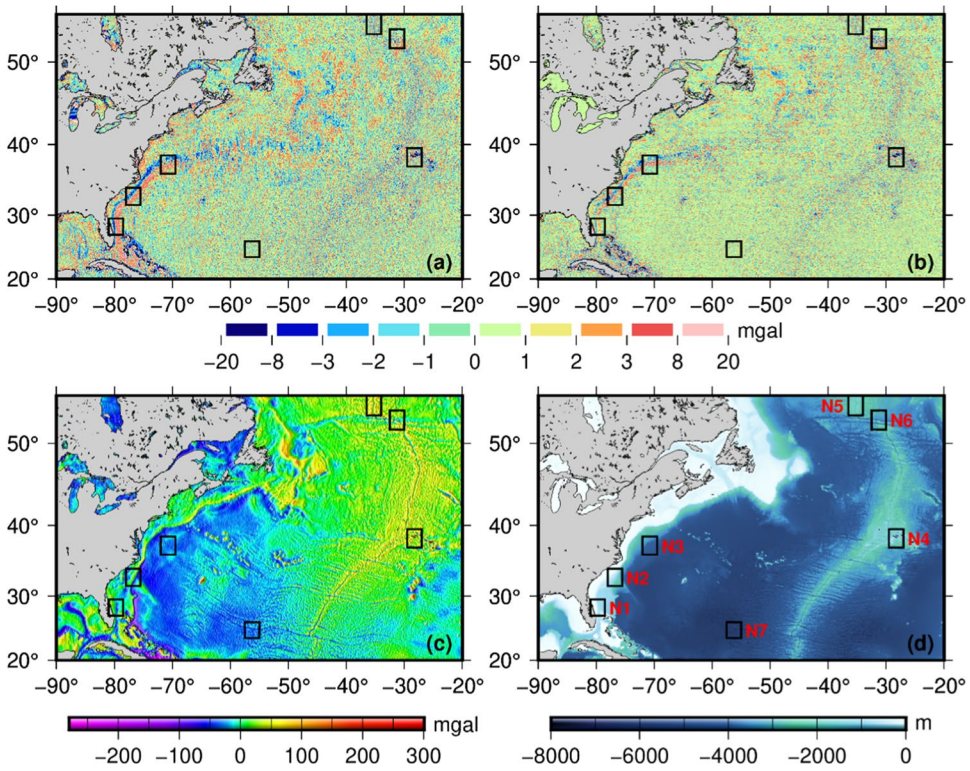

Fig. 4 Residual marine gravity anomalies derived from the SSS-based method (**a**) and the SSH-based method (**b**) over the Northwestern Atlantic area. The subfigures **c**, **d** show the marine gravity anomalies (EGM2008) and ocean depth (GEBCO_2020)

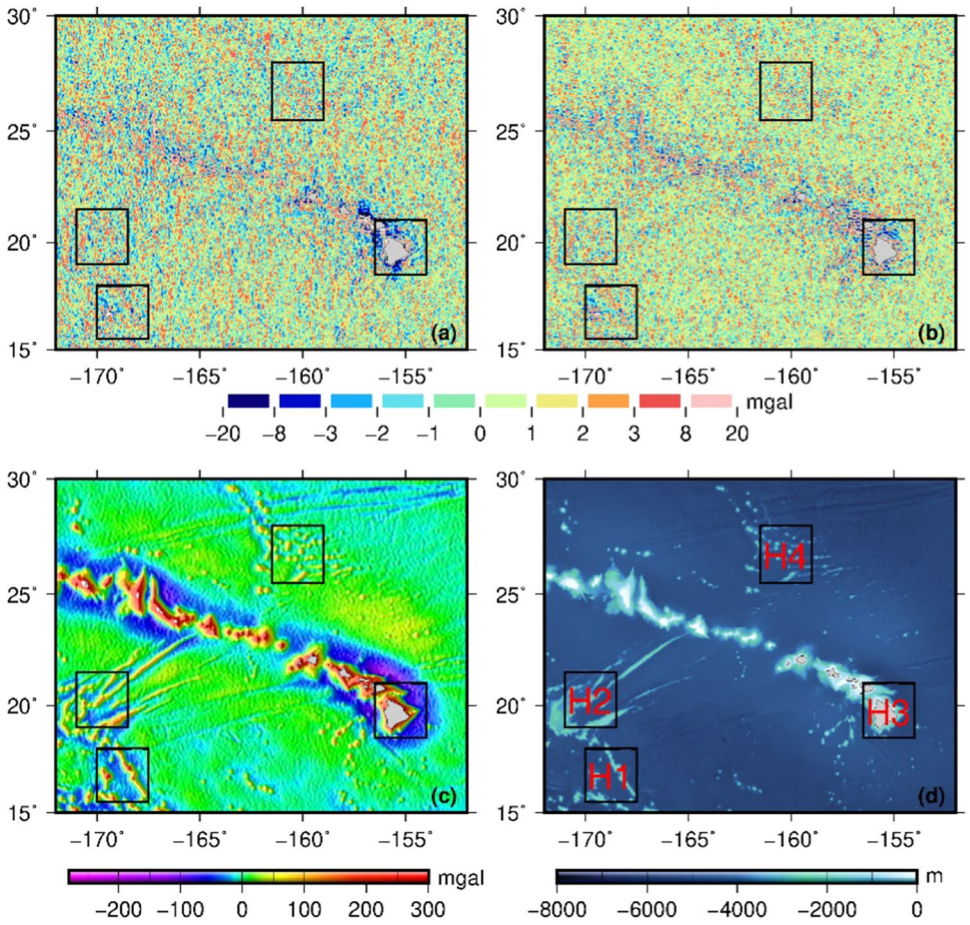

Fig. 5 Residual marine gravity anomalies derived from the SSS-based method (**a**) and the SSH-based method (**b**) over the Hawaii ocean area. The subfigures (**c**, **d**) show the marine gravity anomalies (EGM2008) and ocean depth (GEBCO_2020)

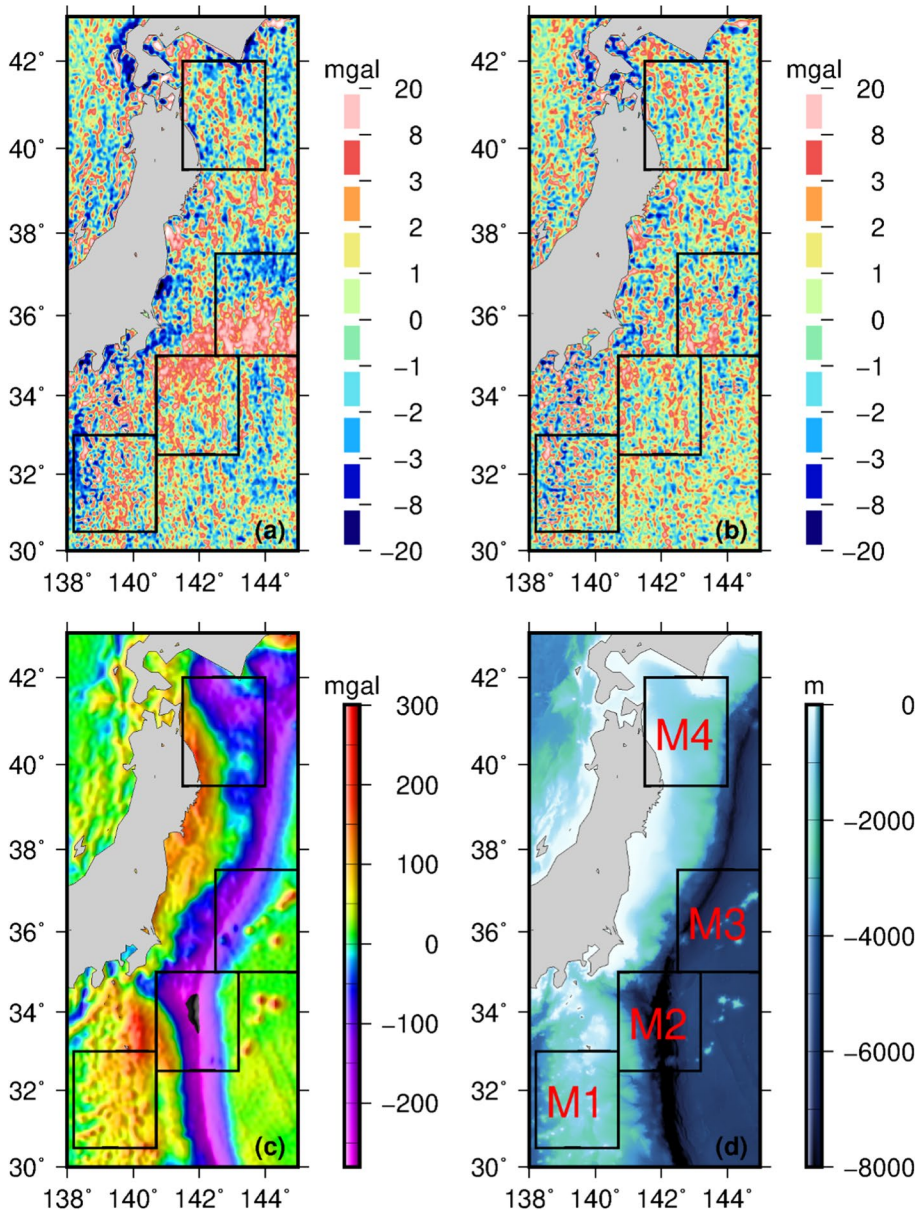

Fig. 6 Residual marine gravity anomalies derived from the SSS-based method (**a**) and the SSH-based method (**b**) over the Mariana Trench area. The subfigures **c**, **d** show the marine gravity anomalies (EGM2008) and ocean depth (GEBCO_2020)

method have short horizontal stripes over the southern Aegean Sea.

As mentioned in Sect. 4.2, we selected small regions by considering diverse characteristics of seafloor topography and sea states, e.g., reefs, seamount, trenches, ocean currents, and so on. We selected 18 rectangular boxes in these study areas, and the statistics within each box are further analyzed. Each chosen region is marked within a black rectangle in these subfigures, and the serial number is marked with red font text in subfigure (d) only. The letter before the number indicates different study areas ('N' for Northwestern Atlantic, 'H' for Hawaii, 'M' for Mariana, and 'A' for Aegean).

For the Northwestern Atlantic, N1 to N3 are selected to show the influence of ocean currents with different flow direction. N4 to N6 represent mid-ocean ridge areas with different directions of the ridge, seamounts, abyssal hills, troughs, and trenches and a strong gravity signal. N7 highlights a deep ocean area with plain seafloor topography and a weak gravity signal. For the Hawaii region, we selected three boxes (H1, H2, and H4) with different directions of bottom topography features. H3 represents a complicated case including the island of Hawaii and its surroundings. For the Mariana Trench area, M1 represents a relatively deep water region with underlying seamounts. M2 shows the influence of the deep trench, which is nearly along the north–south direction. M3 will be influenced by the residual long-wavelength oceanographic signal which is related to Kuroshio. M4 is another coastal comparison. For the Aegean Sea, A1, A2, and A3 are featured

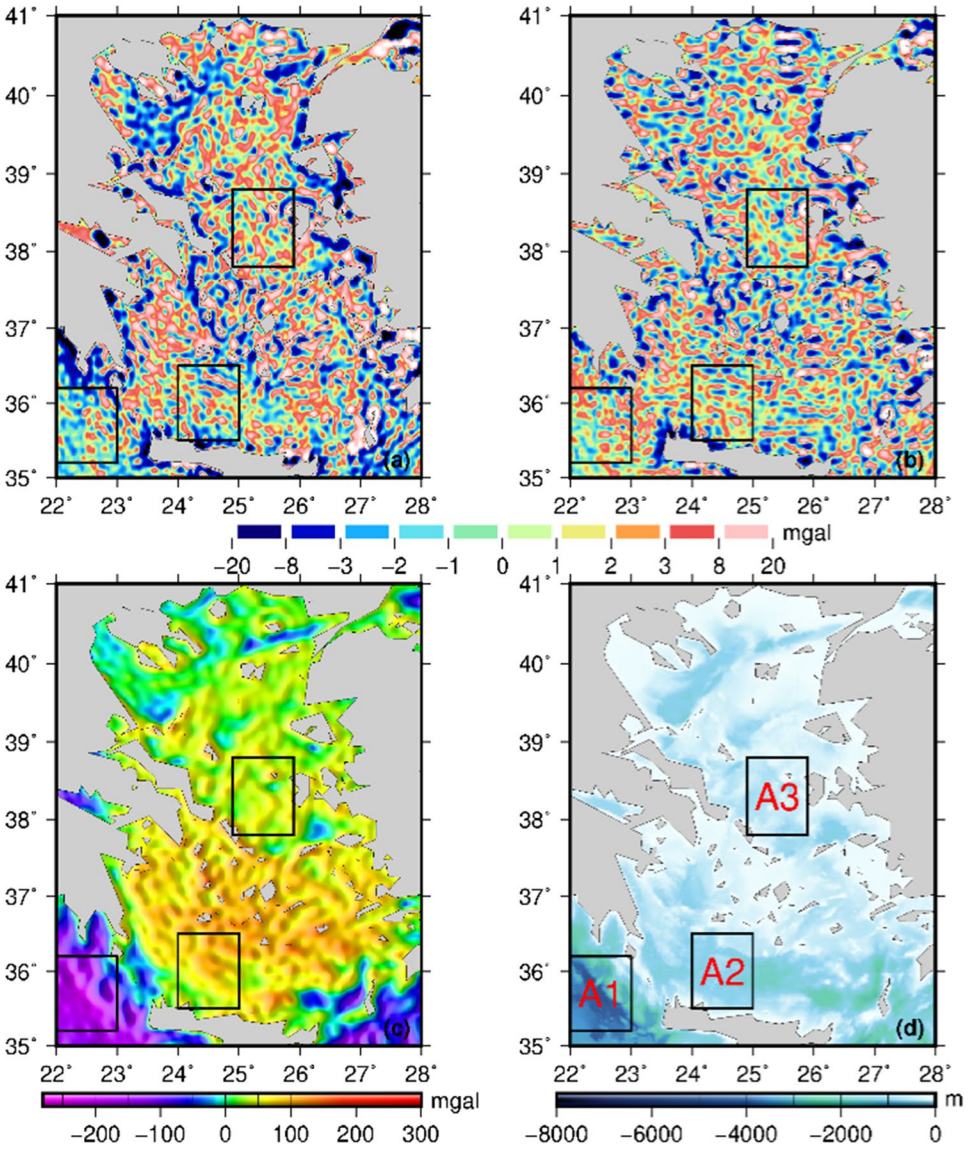

Fig. 7 Residual marine gravity anomalies derived from the SSS-based method (**a**) and the SSH-based method (**b**) over the Aegean Sea area. The subfigures **c**, **d** show the marine gravity anomalies (EGM2008) and ocean depth (GEBCO_2020)

as coastal ocean areas with relatively deep, medium, and shallow water, respectively.

A number of statistics (STD) for height anomalies (=SSH−geoid) and marine gravity signals as well as minimum, maximum, and mean values of ocean depths within entire study regions and selected boxes are shown in Table 5.

As shown in Table 6, the SSH-based method has advantages in coastal regions and shallow water areas (H3, M4, and A2), which is consistent with the conclusions from Tables 3 and 4. The ocean currents (western boundary current) have apparently larger influence on SSS-based methods than the SSH-based method no matter how the flow direction changes (N1, N2, N3, M2). In particular, the accuracy of the SSH-based method is improved by a factor of 1.5 when the direction of the ocean current is nearly north–south (N1).

The SSS-based method has advantages over the deep ocean areas where the seafloor topography features seamounts and ridges (N4, N5, N6, H1, H2, H4, M1, and A1). The advantage of the SSS-based method is more obvious for N6 with the seafloor tectonics (ridges) along the east–west direction which is nearly perpendicular to the orientations of altimeter observations. The SSS-based method also has a better performance over the coastal shallow water region A3, but the amount of marine data for verification is limited.

Moreover, the SSH-based method is superior to the SSS-based method in M2 and M3 over the Mariana Trench area, although these regions are extremely deep with typical bottom topography. The statistics in M2 can be attributed to the approximately north–south directional distribution of the trench, which is almost parallel to the altimeter measurements. The calculation of slopes among adjacent observations along profiles is thus insensitive to detecting this kind of signal variation. The results in M3 are affected by the

Table 5 General information of selected boxes over study area

Ocean area	Number	Long. range Lat. range	STD of height anomaly (m)	STD of gravity (mGal)	Depth range (m)	Mean depth (m)	Comments
Northwestern Atlantic	Entire	270–340 20–55	–	28.59	− 8155 to 2065	− 2861.5	–
	N1	279.0–281.5 27.0–29.5	0.3023	20.63	− 961 to 30	− 387.7	Ocean current (flow north)
	N2	282.0–284.5 31.5–34.0	0.3376	27.73	− 3617 to 9	− 1288.6	Ocean current (flow northeast)
	N3	288.0–290.5 36.0–38.5	0.5161	6.96	− 4627 to − 2807	− 3922.6	Ocean current (flow east)
	N4	330.5–333.0 37.0–39.5	0.1195	27.86	− 3536 to 2065	− 1596.7	Mid-ocean ridge (large residual signal)
	N5	323.5–326.0 53.0–55.0	0.1045	19.29	− 3418 to − 714	− 2134.1	Mid-ocean ridge (north–south ridge)
	N6	327.5–330.0 51.5–53.5	0.1597	26.16	− 4859 to − 824	− 3076.9	Mid-ocean ridge (east–west trench)
	N7	302.5–305.0 23.5–26.0	0.1029	10.58	− 6892 to − 4405	− 5856.7	Abyssal plain (smooth region)
Hawaii	Entire	188.0–208.0 15.0–30.0	–	45.41	− 6849 to 4120	− 4753.5	–
	H1	190.0–192.5 15.5–18.0	0.1191	46.00	− 5558 to 206	− 4473.9	Seafloor topography (northwest-direction)
	H2	189.0–191.5 19.0–21.5	0.1196	36.99	− 5500 to − 939	− 4029.2	Seafloor topography (northeast-direction)
	H3	203.5–206.0 18.5–21.0	0.1263	168.59	− 5835 to 4120	− 3017.1	Sea islands (coastal region)
	H4	198.5–201.0 25.5–28.0	0.1158	18.68	− 5824 to − 1426	− 4662.7	Seafloor topography (east–west direction)
Mariana	Entire	138.0–145.0 30.0–43.0	–	90.46	− 9726 to 3664	− 2724.0	–
	M1	138.2–140.7 30.5–33.0	0.3134	34.29	− 4055 to 301	− 1885.4	Seafloor topography (rapid-change depths)
	M2	140.7–143.2 32.5–35.0	0.2849	122.23	− 9450 to − 931	− 5799.2	Trench (north–south direction)
	M3	142.5–145.0 35.0–37.5	0.4801	71.17	− 8046 to − 1073	− 5754.5	Long-wavelength residual signal
	M4	141.5–144.0 39.5–42.0	0.1512	94.50	− 4995 to 1598	− 1235.7	Coastal (rapid-change depths)
Aegean	Entire	22.0–28.0 35.0–41.0	–	59.97	− 4791 to 2724	− 323.2	–
	A1	22.0–23.0 35.2–36.2	0.0982	51.28	− 4791 to 385	− 3149.6	Deep water
	A2	24.0–25.0 35.5–36.5	0.0854	25.41	− 1768 to 356	− 896.8	Medium depths
	A3	24.9–25.9 37.8–38.8	0.0919	16.84	− 970 to 732	− 448.7	Shallow water

residual long-wavelength signal in observations which is not suitably removed by the reference model, and both methods get lower accuracy.

For a selected box N7 over the Northwestern Atlantic where the seafloor topography is quite smooth and the signal of marine gravity is almost invariant, the two methods produce comparable results and the differences are statistically insignificant.

The above analysis focuses on the numerical match among calculated results and shipborne measurements. A cross-spectral coherence analysis (computed by the Generic Mapping Tools (GMT, Wessel et al. 2013) module *grdfft*) with another bathymetry model (GEBCO_2020) is executed in typical boxes (M1, seamount featured area; H3, coastal area; N2, ocean current area; N7, deep plain ocean area) to further distinguish recovered features for the two methods.

Table 6 Validation information of shipboard data with respect to results derived from two methods and other typical altimetry derived models over selected small regions

Ocean area	Specific region	Count of marine data	SSS-based method	SSH-based method	EGM08	DTU17	V27.1
Northwestern Atlantic	N1	62,051	4.015	2.401	1.744	1.764	4.096
	N2	63,915	2.859	2.336	1.809	1.853	2.668
	N3	6754	3.937	3.839	2.570	3.015	3.933
	N4	5399	3.664	3.836	3.641	3.188	3.389
	N5	1176	2.977	3.134	3.829	3.146	2.906
	N6	1880	3.269	4.101	4.692	3.570	3.105
	N7	2219	2.785	2.748	2.958	2.709	2.689
Hawaii	H1	3096	3.769	3.901	4.267	3.805	3.538
	H2	1450	4.586	4.790	5.411	5.003	4.496
	H3	13,504	8.114	6.968	7.083	6.760	7.921
	H4	2666	4.962	5.190	5.743	5.223	4.931
Mariana	M1	54,823	5.313	5.595	6.375	5.627	4.978
	M2	16,037	5.351	5.281	5.174	5.099	5.226
	M3	5697	7.428	7.301	7.039	7.008	7.163
	M4	4959	6.369	6.351	6.230	6.189	6.314
Aegean	A1	3448	4.158	4.591	5.218	4.703	4.127
	A2	3664	4.686	3.874	5.027	4.419	4.747
	A3	442	4.183	4.666	5.918	5.376	4.157

The first and second columns show different study areas and further selection by the specific rectangular boxes. The third column indicates count of shipboard measurements, accordingly. The last five columns show validation results of shipboard with different grids of gravity anomalies, and the unit is mGal

Figure 8 shows coherence between gravity and bathymetry for significantly different situations. While the seafloor topography features seamount or ridge (e.g., M1), the coherence curves decline to 0.5 at wavelength around 17 km, which is approaching the filter wavelength (16 km) applied to the gravity fields. The SSS-based method has advantages in capturing short wavelength signals within 10–18 km.

The resolution slightly declines to ~ 19 km for seafloor topography features in deep ocean plains (e.g., N7), and the difference between the two methods is still small and negligible, which is consistent with conclusions from Table 6.

In the cases of coastal area or island surroundings (e.g., H3), and ocean currents or high ocean variabilities (e.g., N2), the correlation is weak and the resolution of recovered gravity is limited for both methods. We may consider applying a filter with longer wavelength under these situations or adopt ocean-depth dependent low-pass filter as well in the future.

5 Conclusion

Satellite altimetry provides the most comprehensive images of the marine gravity field with accuracies approaching typical shipboard gravity data. This paper evaluated two marine gravity field recovery methods over four selected geographical areas on the basis of four recent altimeter geodetic missions, Jason-1 GM, Jason-2 GM, SARAL/AltiKa GM, and CryoSat-2 LRM. All these geodetic mission data are uniformly retracked by the two-pass waveform retracker to improve the range precision.

Then, the marine gravity field is determined from the retracked dataset by using both the SSH-based method and the SSS-based method. Results indicate that the SSH-based method has minor advantages in the overall accuracy level because of consistency over both coastal and open ocean areas. The advantage of the SSH-based method is especially prominent over coastal regions. The SSS-based method generally performs better in calculating marine gravity anomalies over the open ocean. The SSS-based method is generally most sensitive to seafloor topography except when the orientation of topography (e.g., trench) is parallel to the orientations of altimeter ground tracks. Also, the SSS-based method is more vulnerable to the energetic western boundary currents, as these generally flow along the direction of ground tracks. In the deep ocean areas where the seafloor topography is plain and smooth, there is no significant difference between the two methods.

SARAL/AltiKa is still running in its geodetic mission and leads to more uneven but dense data distribution across track, from which both methods benefit. Thus, the accuracy of marine gravity will be further improved in the coming years. In addition, the next big step in gravity field improvement may come with the higher range precision and finer

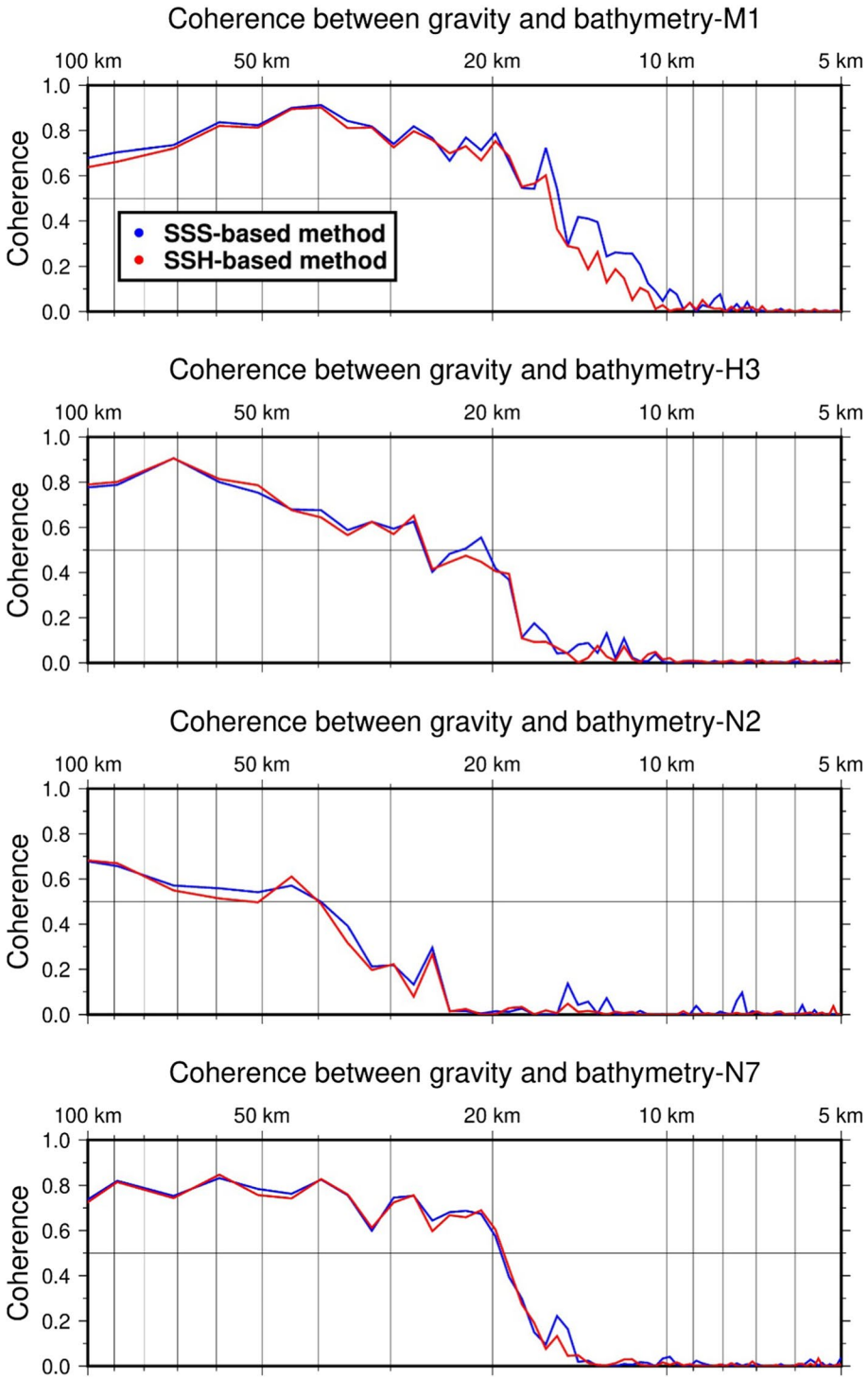

Fig. 8 Coherence between satellite-derived gravity and bathymetry grid (GEBCO_2020) in four typical boxes (M1, H3, N2, and N7). The blue and red curves represent SSS-based result and SSH-based result, respectively

resolution provided by the Surface Water and Ocean Topography (SWOT) mission, which is coming in 2021 (Fu and Ubelmann 2013).

Acknowledgements The multi-satellite altimeter data were provided by CNES and ESA, while the ship-borne gravimetric data were provided by NGA and GEOMED2 project. SIO and DTU kindly proved global marine gravity models for comparison. Zhang is supported by the National Nature Science Foundation of China, Grant No. 41804002, by the State Scholarship Fund of China Scholarship Council, Grant No. 201906085024, by Fundamental Research Funds for the Central Universities.

Author contribution Conception or design of the work was contributed by SZ, AA, and OBA; Data analysis and interpretation were

contributed by SZ, AA, and OBA; Writing—original draft preparation, was contributed by SZ; Writing—review and editing, was contributed by AA and OBA; Critical revision of the article was contributed by DTS; Marine data collection was contributed by JRB.

Data availability The gridded gravity anomalies in NetCDF format for two gravity recovery methods in four research regions will be available via public server (ftp://ftp.space.dtu.dk/pub/Altimetry/Shengjun_MethodComparison).

References

Andersen OB, Knudsen P (1998) Global marine gravity field from the ERS-1 and Geosat geodetic mission altimetry. J Geophys Res 103:8129–8137

Andersen OB, Knudsen P (2019) The DTU17 global marine gravity field: first validation results. In: International association of geodesy symposia, Berlin, Heidelberg. https://doi.org/10.1007/1345_2019_65

Andersen OB, Scharroo R (2011) Range and geophysical corrections in coastal regions: and implications for mean sea surface determination. In: Vignudelli S, Kostianoy A, Cipollini P, Benveniste J (eds) Coastal altimetry. Springer, Berlin, pp 103–146

Andersen OB, Knudsen P, Berry PAM (2010) The DNSC08GRA global marine gravity field from double retracked satellite altimetry. J Geod 84(3):191–199

Andersen OB, Knudsen P, Kenyon S, Holmes S (2014) Global and Arctic marine gravity field from recent satellite altimetry (DTU13). In: Proceedings 76th EAGE conference and exhibition 2014, Amsterdam RAI, the Netherlands. http://doi.org/https://doi.org/10.3997/2214-4609.20140897

Barzaghi R, Carrion D, Pepe M, Prezioso G (2016) Computing the deflection of the vertical for improving aerial surveys: a comparison between EGM2008 and ITALGEO05 estimates. Sensors 16(8):1168

Barzaghi R, Carrion D, Vergos GS, Tziavos IN et al (2019) GEOMED2: high-resolution geoid of the mediterranean. In: Sánchez L, Freymueller JT (eds) International symposium on advancing geodesy in a changing world—proceedings of the IAG scientific assembly. International Association of Geodesy Symposia, vol 149. Springer, pp 43–49

Brown G (1977) The average impulse response of a rough surface and its applications. IEEE Trans Antennas Propag 25:67–74

Catalao J (2006) Iberia-Azores Gravity Model (IAGRM) using multisource gravity data. Earth Planets Space 58(3):277–286

Featherstone W, Holmes S, Kirby JF, Kuhn M (2004) Comparison of remove-compute-restore and university of new brunswick techniques to geoid determination over Australia, and inclusion of wiener-type filters in reference field contribution. J Surv Eng 130:1. https://doi.org/10.1061/(ASCE)0733-9453(2004)130:1(40)

Forsberg R, Tscherning CC (1981) The use of height data in gravity field approximation by collocation. J Geophys Res Solid Earth 86(B9):7843–7854

Fu L-L, Cazenave A (2001) Satellite altimetry and earth sciences: a handbook of techniques and applications. Academic, San Diego

Fu LL, Ubelmann C (2013) On the transition from profile altimeter to swath altimeter for observing global ocean surface topography. J Atmos Ocean Technol 31:560–568

Garcia ES, Sandwell DT, Smith WHF (2014) Retracking CryoSat-2, Envisat, and Jason-1 radar altimetry waveforms for improved gravity field recovery. Geophys J Int 196(3):1402–1422

GEBCO Bathymetric Compilation Group 2020 (2020) The GEBCO_2020 Grid—a continuous terrain model of the global oceans and land. British Oceanographic Data Centre, National Oceanography Centre, NERC, UK. https://doi.org/10.5285/a29c5465-b138-234d-e053-6c86abc040b9

Green CM, Fletcher KMU, Cheyney S, Dawson GJ, Campbell SJ (2019) Satellite gravity—enhancements from new satellites and new altimeter technology. Geophys Prospect 67(6):1611–1619

Harrison JC (1955) An Interpretation of Gravity Anomalies in the Eastern Mediterranean. Philos Trans R Soc Lond Ser A Math Phys Sci 248(947):283–325

Hofmann-Wellenhof B, Moritz H (2005) Physical geodesy. Springer, Berlin. ISBN: 3211274677, 9783211274675

Hwang C (1998) Inverse Vening Meinesz formula and deflection-geoid formula: applications to the predictions of gravity and geoid over the South China Sea. J Geodesy 72:304–312

Hwang C, Hsu H, Jang R (2002) Global mean sea surface and marine gravity anomaly from multi-satellite altimetry: applications of deflection-geoid and inverse Vening Meinesz formulae. J Geod 76:407–418

Khaki M, Forootan E, Sharifi M, Awange J, Kuhn M (2015) Improved gravity anomaly fields from retracked multimission satellite radar altimetry observations over the Persian Gulf and the Caspian Sea. Geophys J Int 202(3):1522–1534

Knudsen P, Brovelli M (1993) Collinear and cross-over adjustment of geosat erm and seasat altimeter data in the mediterranean sea. Surv Geophys 14(4–5):449–459

Li J, Sideris M (1997) Marine gravity and geoid determination by optimal combination of satellite altimetry and shipborne gravimetry data. J Geodesy 71:209–216

Lu B, Barthelmes F, Li M, Förste C et al (2019) Shipborne gravimetry in the Baltic Sea: data processing strategies, crucial findings and preliminary geoid determination tests. J Geodesy 93:1059–1071

McAdoo DC, Farrell SL, Laxon S, Ridout A, Zwally HJ, Yi D (2013) Gravity of the Arctic Ocean from satellite data with validations using airborne gravimetry: oceanographic implications. J Geophys Res Ocean 118(2):917–930

Olgiati A, Balmino G, Sarrailh M, Green CM (1995) Gravity anomalies from satellite altimetry: comparison between computation via geoid heights and via deflections of the vertical. Bull Géodésique 69(4):252–260

Pavlis NK, Holmes SA, Kenyon SC, Factor JK (2012) The development and evaluation of the earth gravitational model 2008 (EGM2008). J Geophys Res V117:B04406. https://doi.org/10.1029/2011JB008916

Sandwell DT, Smith WHF (1997) Marine gravity anomaly from Geosat and ERS-1 satellite altimetry. J Geophys Res 102:10039–10054

Sandwell DT, Smith WHF (2005) Retracking ERS-1 altimeter waveforms for optimal gravity field recovery. Geophys J Int 163(1):79–89

Sandwell DT, Smith WHF (2009) Global marine gravity from retracked Geosat and ERS-1 altimetry: ridge segmentation versus spreading rate. J Geophys Res 114(B1):B01411

Sandwell DT, Garcia ES, Soofi K, Wessel P, Chandler M, Smith WHF (2013) Towards 1-mGal accuracy in global marine gravity from Cryosat-2, Envisat and Jason-1. Lead Edge 32:892–898

Sandwell DT, Müller RD, Smith WHF et al (2014) New global marine gravity model from CryoSat-2 and Jason-1 reveals buried tectonic structure. Science 346(6205):65–67

Sandwell DT, Harper H, Tozer B, Smith WHF (2019) Gravity field recovery from geodetic altimeter missions. Adv Space Res. https://doi.org/10.1016/j.asr.2019.09.011

Schwarz K, Sideris M, Forsberg R (1990) The use of fft techniques in physical geodesy. Geophys J Int 100(3):485–514

Stammer D, Cazenave A (ed) (2017) Satellite altimetry over oceans and land surfaces. CRC Press, Boca Raton. https://doi.org/10.1201/9781315151779

Stenseng L, Andersen OB (2012) Preliminary gravity recovery from CryoSat-2 data in the Baffin Bay. Adv Space Res 50(8):1158–1163

Wessel P, Smith WHF, Scharroo R, Luis JF, Wobbe F (2013) Generic mapping tools: improved version released. EOS Trans AGU 94:409–410

Yildiz H, Forsberg R, Ågren J, Tscherning CC, Sjöberg LE (2012) Comparison of remove-compute-restore and least squares modification of Stokes' formula techniques to quasi-geoid determination over the Auvergne test area. J Geodetic Sci 2(1):53–64

Zaki A, Mansi AH, Selim M, Rabah M, Fiky GE (2018) Comparison of satellite altimetric gravity and global geopotential models with Shipborne gravity in the red sea. Mar Geodesy 41(3):258–269

Zhang S, Sandwell DT (2017) Retracking of SARAL/AltiKa radar altimetry waveforms for optimal gravity field recovery. Mar Geodesy 40(1):40–56

Zhang S, Sandwell DT, Jin T, Li D (2017) Inversion of marine gravity anomalies over southeastern China seas from multi-satellite altimeter vertical deflections. J Appl Geophys 137:128–137

Zhang S, Li J, Jin T, Che D (2018) Assessment of radar altimetry correction slopes for marine gravity recovery: a case study of Jason-1 GM data. J Appl Geophys 151:90–102

Zhang S, Andersen OB, Kong X, Li H (2020) Inversion and validation of improved marine gravity field recovery in South China Sea by incorporating HY-2A altimeter waveform data. Remote Sens 12:802

Zhu C, Guo J, Hwang C et al (2019) How HY-2A/GM altimeter performs in marine gravity derivation: assessment in the South China Sea. Geophys J Int 219:1056–1064

Zhu C, Guo J, Gao J, Hwang C et al (2020) Marine gravity determined from multi-satellite GM/ERM altimeter data over the South China Sea SCSGA V10. J Geodesy 94:50